CrossMark

The effect of surface finish on tensile behavior of additively manufactured tensile bars

Wes Everhart[1] · Eric Sawyer[1] · Tod Neidt[1] · Joe Dinardo[1] · Ben Brown[1]

Abstract Additive Manufacturing (AM) has significantly increased the design freedom available for metal parts. Many novel designs rely on the existence of surfaces that are not accessible and therefore rely on the surface finish of the parts directly from the AM equipment. Work has been performed to characterize the difference between AM, then machined tensile samples and AM tensile samples with an unimproved surface finish. This work utilizes surface analysis, fractography, and finite element analysis (FEA) to expand on this by investigating the effects of the unimproved surfaces on local tensile behavior and fracture mechanics in AM materials. Results show that measurement error in cross-sectional area is the main source of variation between unfinished and machined strength measurements. Results also indicate that a ductile material may demonstrate the same tensile strength regardless of post processing. Fractography shows that stress concentration near the surface of the samples leads to changes in fracture behavior likely explaining the difference in elongation of the samples. Finally, FEA work did not successfully show a difference in fracture initiation, though this is likely due to inaccurate representation of the samples surface.

Introduction

Recent growth in the use of AM metals has brought to light the need to understand the behavior of these materials under stress. There have been several studies to investigate the strength of various additively manufactured metals including titanium, nickel, iron, aluminum, and cobalt-based alloys [1–11]. In many of these publications, one or more factors that can affect the properties of interest are not accounted for, often including build parameters, orientation, post processing, etc.

Many of these studies focus on test orientation relative to the build direction, and the results are mixed [12–18]. Some demonstrate variance in yield strength and tensile strength, while others indicate only a change in ductility. All studies surveyed indicate that samples tested parallel to the build direction have strength less than or equal to samples tested perpendicular to the build direction. In these studies, the variation of build direction along with limitations in the capabilities of many AM processes to produce unsupported overhang geometries forces samples to be built as blocks and then machined to their final shape. While providing accurate information about the material properties produced during the bulk material fill sequence of a build, these machined samples do not provide information about the properties of contour passes, and perhaps more importantly, they do not account for any change in performance that could be caused by the rough AM surface finish. These effects are important to understand as the economic viability of AM processes often depends on the minimization of post processing, thus potentially placing regions with unfinished surfaces under load.

A small number of studies have investigated the difference in tensile properties between samples with unimproved surface finish and samples machined to meet ASTM E8. In a recent study by Rafi et al. [19], cylindrical Ti–6Al–4V tensile bars were fabricated on both laser and electron beam powder bed systems. Samples were built both vertically and horizontally, and with both unfinished and machined surface finishes. The horizontal bars with unfinished surfaces appear to be built without supports and

✉ Wes Everhart
weverhart@kcp.com

[1] National Security Campus, Kansas City, MO 64147, USA

likely have some dimensional inaccuracy and extreme surface variation due to melt pool inconsistency in unsupported regions. Relevant to this work, it was found that the vertically oriented parts exhibited lower tensile properties and that, in general, the machined bars showed improved performance over those in the unfinished condition. The authors focused on microstructural variance to discuss the tensile property variance. Niendorf and Brenne [20] studied flat tensile bars of TWIP steel, which were fabricated in a single orientation using supports. Samples were tested at multiple points during post processing, after electro-discharge machining to remove supports, after surface grinding, and after heat treatment. Samples showed variation in strength and ductility; specifically, there was a reduction in strengths of the AM parts when compared to conventionally processed sheet material. This difference, for both the unfinished samples and the samples with a ground surface, was attributed to error in measurement of the sample cross section caused by the rough surface.

Few resources were found that discussed the effect of surface finish on tensile properties. There have been publications investigating the effect of surface finish on the behavior of metals under various circumstances that utilized FEA. Suh et al. [21] studied the effect of sample thickness and surface roughness on the tensile properties of aluminum sheet products. They intended to vary the surface roughness of their samples; however, they found it was difficult to control the specimen surface roughness with the chemical etching method they used to vary thickness. As a substitute, they developed periodic surface roughness in their FEA models in an attempt to approximate the variation in surface finish. They showed that surface roughness reduced both strength and ductility. Chen et al. [22] studied the impact of surface finish on nano-indentation results. Random functions were used in Matlab to create different surfaces for FEA simulation. One study did find success in capturing the surface finish of real samples with laser imagery and implementing that measured surface in an FEA simulation [23]. Unfortunately, the study concentrated on asymmetric rolling and associated contact and friction and not directly on tensile behavior.

This study intends to evaluate the difference in the tensile behavior of additively manufactured parts that have an unimproved surface and those that have been machined to meet ASTM E8. Evaluation will cover selective laser melting (SLM) of 17 PH SS and electron beam melted (EBM) Ti–6Al–4V and will utilize tensile testing, CMM, microstructural analysis, fractography, and FEA.

Materials and methods

All additive builds consisted of a grid of vertical 4.0 mm diameter tensile bars spaced 40 mm apart with geometry as shown in Fig. 1. Vertical samples were chosen as an indication of minimum properties based on the previous work discussed above and a diameter of 4.0 mm was chosen to provide a representative size of product that would be economical to produce using additive manufacturing. This size range is expected to provide a realistic probability for defects in the applied processes though ductility results may be skewed.

In this work, all Ti–6Al–4V test specimens were prepared using an Arcam A2X and Arcam supplied Ti–6Al–4V plasma spheroidized powder with a normal distribution between 45 and 105 μm. A complete and detailed description of EBM theory and the Arcam A2X is too lengthy to describe here; however, some relevant details will be provided as these are pertinent to the design of experiments and are typically not provided in other previously reported work. An accelerating voltage of 60 kV is applied, and during the build a vacuum level of approximately 2×10^{-3} mBar is

Fig. 1 Build geometries used in both SLM and EBM systems. Unfinished tensile geometry (*left*) and overall build geometry set up (*right*)
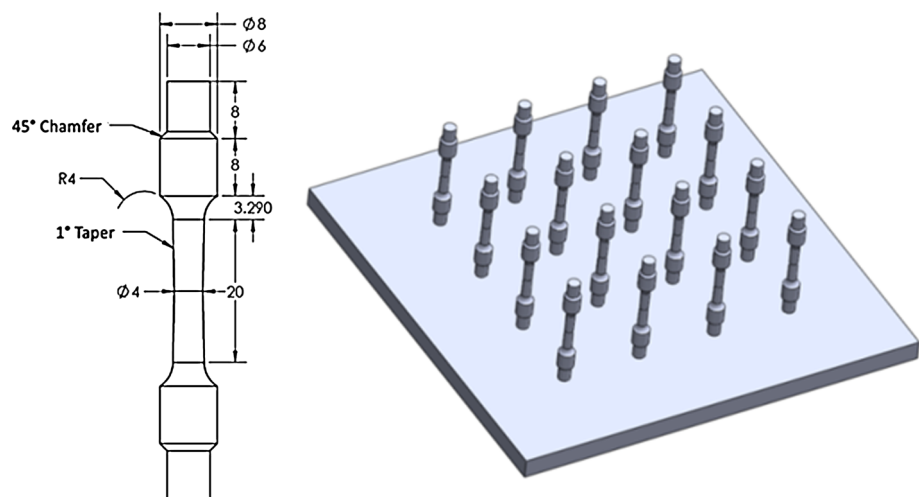
maintained by machine control software. For this work, EBM Control Software Version 3.2.132 using Standard Arcam Ti–6Al–4V 50 μm layer thickness theme version 3.2.121 was used. Beam focus offset is a machine setting that is subject to vary from machine to machine and is set during beam calibration procedures. For this study, a focus offset value of 1 mA was used.

The 17–4 PH stainless steel test specimens were prepared using an EOS M280 and EOS supplied GP1 gas atomized powder with a normal distribution between 15 and 45 μm. An inert nitrogen build environment was produced with the on-machine nitrogen generator and oxygen was maintained below 0.1 %. The build platform heater was used to maintain a platform heat of 170 C. For this work, the following custom build parameters were used: beam energy of 310W, hatch spacing of 100 μm, beam speed of 2754 mm s^{-1}, and a layer thickness of 50 μm.

Tensile properties of the AM samples were determined per ASTM E8 [24] under room temperature conditions. Modulus of elasticity, 0.2 % offset yield strength, tensile strength, elongation, and reduction of area were measured. For the unimproved specimens, the cross-sectional area within the gage section was captured through three measurements of diameter recorded at 120° intervals which were averaged for the calculation of cross-sectional area to account for any non-uniformity in roundness and the high surface roughness. All machined gage sections followed the ASTM specification for measurement of the test diameter. Crosshead test speeds were controlled uniformly to minimize any impact of rate sensitivity, and the loading rates were approximately 620 MPa min^{-1}. The test machines and extensometers met ASTM E4 [25] and ASTM E83 [26] specifications, respectively.

For more robust characterization of the surface profile of the unimproved samples, laser analysis was considered according to Xie et al. [23]; however, the method could not be applied to the round sample surface. Instead, CMM inspection was performed on a Zeiss Prismo CMM with ±0.0023 mm accuracy. The stylus used had a 0.0457 mm radius. This inspection was done on two 17–4 PH samples and two Ti–6Al–4V samples. First, points were taken around the centerline circumference of the tensile bar at every one degree of rotation. This process was repeated again at five different locations spaced 0.635 mm apart on each side of the tensile centerline. These points were then loaded into CAD software, and a geometry was created by fitting splines to each series of vertical points and then blending those splines together.

For simulation of the modeled tensile bars, the tensile gage section geometry is quartered and then separately meshed to reduce simulation time. The hexahedron mesh size was approximately 0.051 mm. This essentially creates four tensile bars out of one when quarter-symmetry

boundary conditions are imposed on the cut surfaces. Two surface nodes are assigned to separate node sets to act as the extensimeter on the tensile bar. The stress–strain curve from the machined tensile bar test samples is converted to true stress and true strain values for input into the plastic portion of the material model. Young's Modulus is taken from the test sample lab report to inform the elastic region of the material model. It should be noted that the machined samples no longer have material that was melted under contour parameters which are different from fill parameters. This may contribute to a difference in properties when examining unfinished samples; however, for these samples, less than 5 % of the cross-sectional area is melted with contour parameters, so any effect is limited. The remaining material model parameters are populated with data from the Metallic Materials Properties Development and Standardization database for material properties using annealed Ti–6Al–4V and annealed 17–4 PH stainless Steel [27]. It should be noted that the potential residual stresses existing in the samples are ignored in the simulation. While this is likely a sound assumption for the electron beam process due to its high temperature, distortion due to residual stresses has been observed on material built using the laser process. The virtual tensile bars are "pulled" using Sierra Adagio Solid Mechanics Implicit FEA code. A kinematic displacement boundary condition is applied to the top surface of the tensile bar geometry, while a fixed displacement boundary condition holds the bottom surface of the geometry in place. Quarter-symmetry boundary conditions are used on the cut surfaces of the tensile bar geometry. Each bar is pulled far enough to induce necking in the geometry. Displacement of the two gage nodes and a sum of the reaction forces on the fixed surface is recorded as history output. Displacements, Von Mises stress, and equivalent plastic strain (EQPS) variables are recorded as field output. The history file containing gage node displacements and reaction force are saved and imported into Excel for processing. These simulation outputs are representative of the physical force versus displacement outputs generated by the experimental tensile test and are processed as if they are physical. First the difference between the gage nodes is taken and converted into a strain value. The reaction force variable is multiplied by four to account for the quarter-symmetry assumption and then divided by the original surface area to give stress. These values are used in true stress and true strain calculations up to the maximum engineering stress value.

Results

The caliper measurement technique for evaluating the cross-sectional area under load in the tensile testing process produced relatively uniform results (Table 1). The 17–4

PH unfinished samples showed a more consistent measurement at each angle indicating they have a high roundness; however, those samples were much larger than the nominal 4.0 mm diameter of the model. The Ti–6Al–4V samples measured much closer to the nominal diameter, but had a much higher standard deviation indicating that they were less round. In general, the 17–4 PH samples are significantly smoother than the Ti–6Al–4V samples, and the surface roughness is largely caused by a random distribution of adhered particles.

The CMM measurement results for the unfinished 17–4 PH samples again showed a larger nominal diameter and a high average roundness value of 0.048 mm, while the unfinished Ti–6Al–4V samples have a smaller diameter and an average roundness number of 0.134 mm. For the purposes of evaluating the impact of surface finish on the performance of a tensile bar, several cross-sectional area calculations were performed. The first three are simple circular approximations using the minimum, mean, and maximum diameters from the CMM results. The fourth is the triangulated cross-sectional area which is an approximation based on the area calculated from the FEA mesh of each entire sample. It can be seen in Table 2 that in both sets of unfinished samples, the mean Area and triangulated Area are very similar. When compared to the experimental results, the 17–4 PH Mean Area matches very well, and the Ti–6Al–4V experimental results are slightly larger than their Mean Area. This difference is likely due to the difference in roundness. Additionally, the unfinished Ti–6Al–4V samples showed significantly higher surface roughness when compared to the 17–4 PH samples.

The experimental results from the tensile tests are summarized in Table 3. The yield strength of the 17–4 PH samples showed a 12.2 % increase when the surface was

Table 1 Tensile sample caliper measurements of diameter

Sample ID	Condition	Diameter 1 (mm)	Diameter 2 (mm)	Diameter 3 (mm)	Average diameter (mm)	Standard deviation (mm)	Calculated area (mm^2)
17–4 PH SN2	Unfinished	4.133	4.130	4.138	4.133	0.004	13.42
17–4 PH SN3	Unfinished	4.117	4.115	4.115	4.116	0.001	13.30
17–4 PH SN4	Machined	3.993	N/A	N/A	3.993	N/A	12.52
Ti–6Al–4V SN8	Unfinished	4.031	4.059	4.021	4.037	0.019	12.80
Ti–6Al–4V SN10	Unfinished	4.003	4.039	3.988	4.010	0.026	12.63
Ti–6Al–4V SN2	Machined	4.006	N/A	N/A	4.006	N/A	12.60

Table 2 Tensile test results from both unfinished and machined samples

Sample ID	Condition	Experimental Calculated area (mm^2)	Meshed model (CMM)			
			Min area (mm^2)	Mean area (mm^2)	Max area (mm^2)	Triangulated area (mm^2)
17–4 PH SN2	Unfinished	13.42	12.52	13.36	14.70	13.33
17–4 PH SN3	Unfinished	13.30	12.52	13.36	14.61	13.33
Ti–6Al–4V SN8	Unfinished	12.80	11.13	12.39	14.43	12.36
Ti–6Al–4V SN10	Unfinished	12.60	11.03	12.35	13.84	12.33

Table 3 Tensile test results from both unfinished and machined samples

Sample ID	Condition	Yield strength (MPa)	Ultimate tensile strength (MPa)	Elongation (%)	Reduction of area (%)
17–4 PH SN2	Unfinished	473.7	873.6	41.5	65.6
17–4 PH SN3	Unfinished	479.2	879.1	41.1	66.4
17–4 PH SN4	Machined	535.0	881.8	51.6	67.8
Ti–6Al–4V SN8	Unfinished	817.7	904.6	8.2	28.7
Ti–6Al–4V SN10	Unfinished	812.9	900.5	7.3	23.7
Ti–6Al–4V SN2	Machined	987.3	1103.2	15.0	33.9

machined to ASTM E8, though the ultimate tensile strength was not significantly increased. Similarly, the percent elongation was increased by 24.9 % and the reduction of area showed no change. The Ti–6Al–4V samples showed an increase in yield strength and tensile strength of 21.1
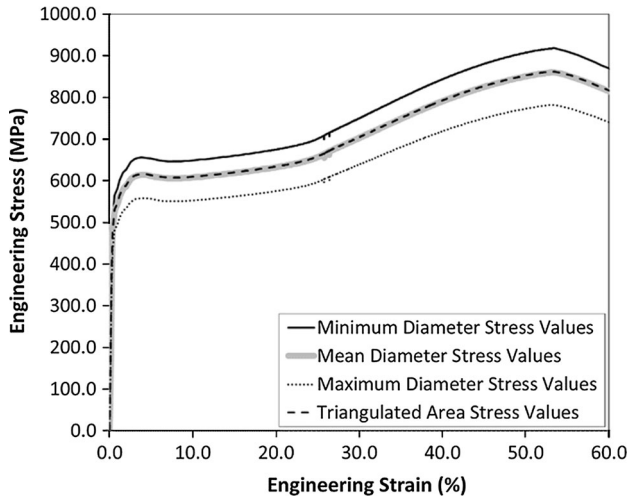

Fig. 2 Simulation results for 17–4 PH SN 2 for the minimum, mean, and maximum diameter values from the model as well as the triangulated area from the mesh

and 22.23 %, respectively, while percent elongation and reduction of area were reduced by 93.6 and 29.4 %.

The stress and strain FEA calculations performed on the maximum nodal displacements and reaction force along with the various approximations of cross-sectional area (Table 2) were used to create stress–strain curves. The results of this analysis show a simple scaling of the same curve relative to the change in cross-sectional area used in the stress calculation, as shown in Fig. 2.

Analysis of the stress values of individual elements in the model showed stress concentrations at the surface of the unfinished tensile bars (Fig. 3). These stress concentrations appear in areas of smaller relative diameter and appear to have a reduced effect as global strain increases in the 17–4 PH simulation, but a sustained effect in the Ti–6Al–4V simulation. Stress maps also show that no significant stress concentration occurred at the symmetry boundaries indicating that quarter symmetry used in FEA did not alter the results.

Discussion

It seems fairly obvious that error in the measurement of the cross-sectional area would cause some error in the measurement of yield strength and ultimate tensile strength.
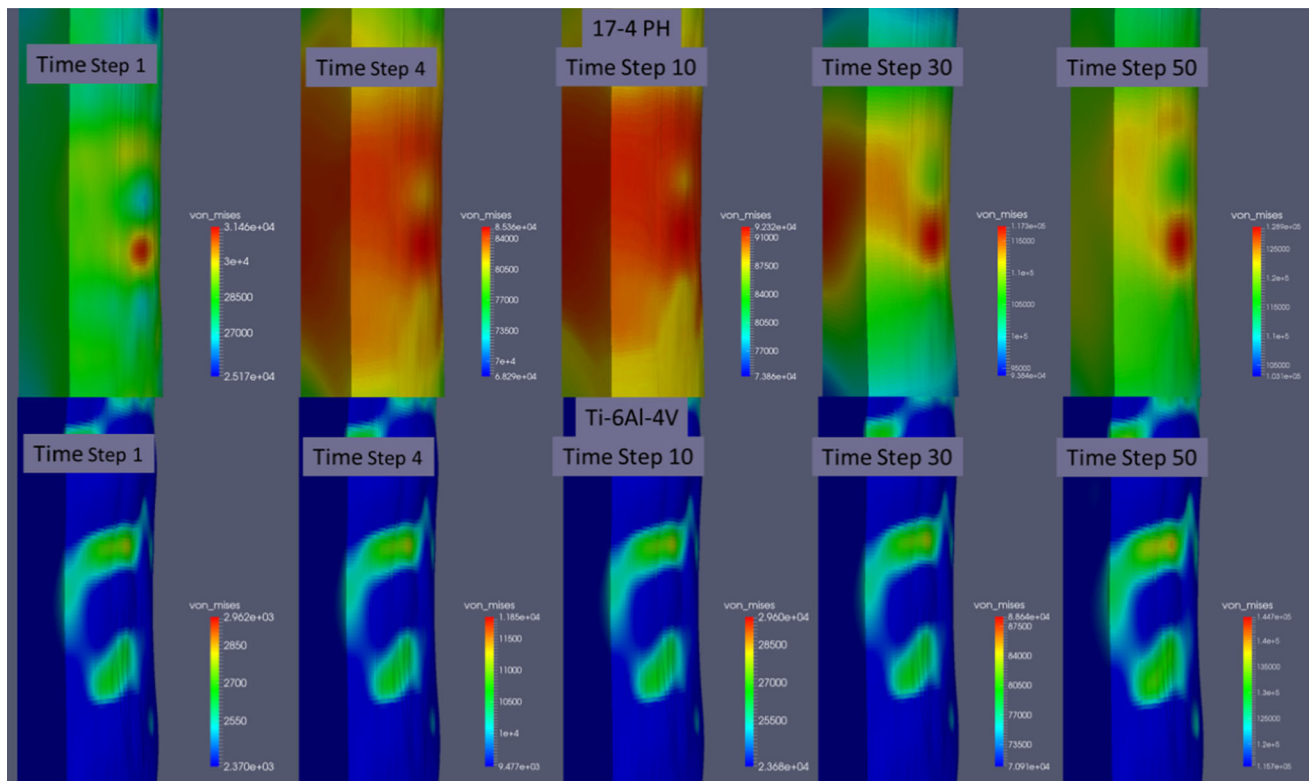

Fig. 3 A comparison of surface stress concentration during the tensile test for unfinished 17–4 PH and Ti–6Al–4V samples. *The color scale* at each time step represents the highest 20 % of stress values to emphasize and stress concentrations and progress into the plastic strain region
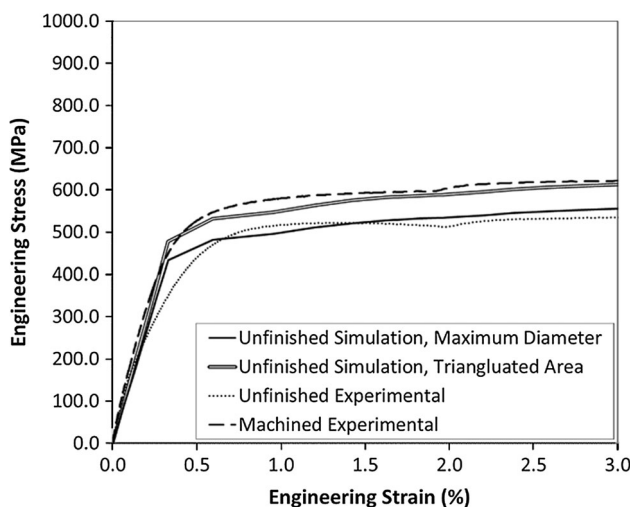
Fig. 4 Comparison of simulation results and experiment results for low-strain values of 17–4 PH SN2

Figure 4 shows that during elastic deformation and the early stages of plastic deformation, the 17–4 PH machined experimental results follow closely with the unfinished mean diameter simulation.

The unfinished tensile bar experimental results show good correlation with the unfinished tensile bar simulation using cross-sectional area calculated from the maximum diameter. It is reasonable to expect that the values measured with calipers (unfinished experimental results) are similar to the unfinished maximum diameter simulation indicating that a simple adjustment of the cross-sectional area to account for measurement error would bring the two experimental results into agreement. This theory is put to the test when the remainder of the plastic region of the curves is considered (Fig. 5). The machined experimental results continue to match well with the mean cross-sectional area. The unfinished sample, however, reaches nearly the same ultimate tensile strength as the machined sample.
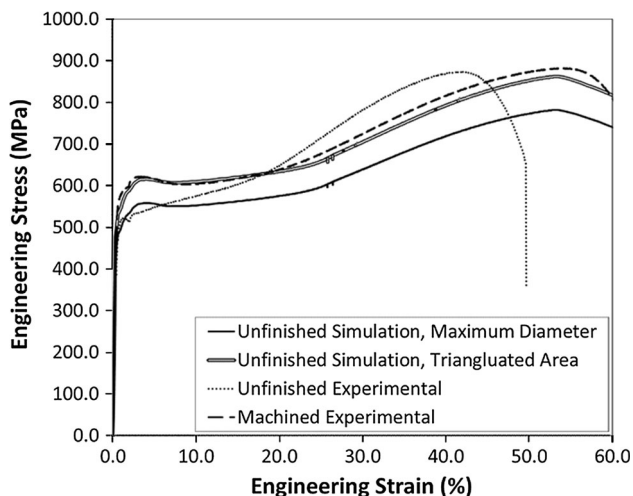
If the cross-sectional area difference remains at high strains, then the unfinished samples have higher tensile strength than the machined samples, though this is unlikely. As indicated by the reduction of stress concentration seen in the tensile bar simulations (Fig. 3), the surface appears to smooth as strain increases which would change the error in cross-sectional area measurement and redistribute load within the sample altering the tensile behavior.

Also of note in Fig. 5 is the fact that the unfinished sample strain hardens at a faster rate and fails at a lower percent elongation than the unfinished simulation. This difference cannot be due to measurement error in cross-sectional area as this value has no impact on the measurement of elongation and strain in a tensile test. Similar to the 17–4 PH, results in Figs. 4, 6 show a strong correlation of both the T–6Al–4V machined sample with the mean diameter simulation results and the unfinished sample with the maximum diameter simulation for low strains.

When expanded to large strains, as shown in Fig. 7, the same analysis applies though there is a difference in morphology of the curve in the region just after yielding. In the actual tensile test, the strain rate is increased after yielding to improve lab efficiency. This increase in strain rate activates additional deformation twinning which increases the strength of the material. Since the behavior of each individual element is governed by the curve generated from the machined sample, the difference in morphology of this region is due to the gradual increase of elements which are
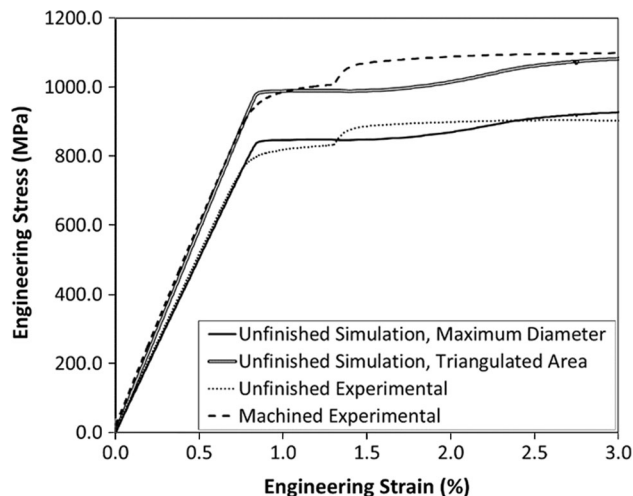

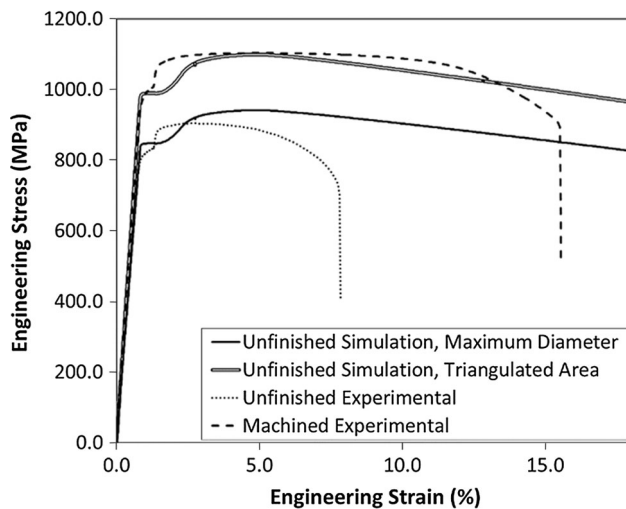**Fig. 5** Comparison of simulation results and experimental results for high-strain values of 17–4 PH SN2

Fig. 6 Comparison of simulation results and experimental results for low-strain values of Ti–6Al–4V SN8

Fig. 7 Comparison of simulation results and experimental results for high-strain values of Ti–6Al–4V SN8

smoothing, high-tensile strength, and increased rate of work hardening exhibited in the 17–4 PH samples indicate a change in tensile behavior of materials with high ductility. Essentially, such materials appear to be able to overcome some level of surface roughness through local plastic deformation. Similar to the 17–4 PH, the unfinished Ti–6Al–4V samples exhibited much lower elongation than the simulation predicted.

To analyze potential microstructural variations at the surface of each sample caused by the removal of the unfinished surface on the machined samples, structures near the center and toward the edge of the unfinished samples were compared. Figure 8 shows that the region governed by the contour scans in the 17–4 PH materials exhibits a larger grain size when compared to the material in the center of the part. The Ti–6Al–4V sample shows no significant change in structure near the edge. This variation may contribute to the altered strain rate observed in the 17–4 PH unfinished sample, though the relatively small percentage of the cross-sectional area that is affected reduces the likelihood of such an effect.

In an attempt to account for the difference in elongation in each sample set, two methods were incorporated to indicate the initiation of fracture. First, a failure criteria (ε_{crit}) for the model is calculated from of the reduction of area (ROA) for the test sample, as shown in Eq. 1.
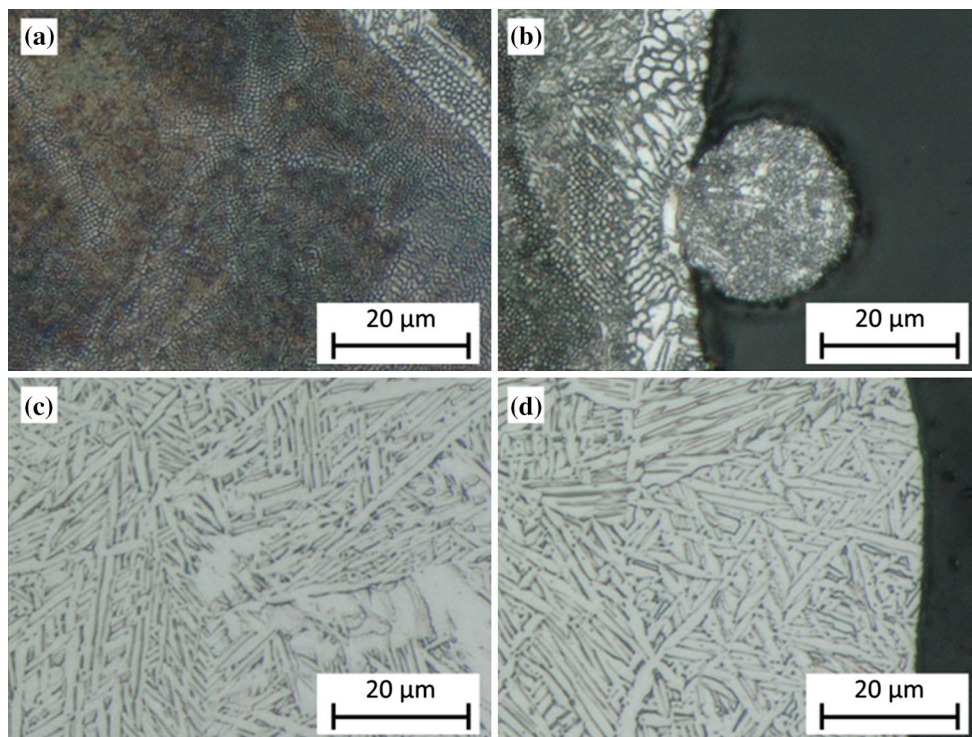
reaching the high-strain rate region as opposed to the immediate onset in the actual test. For the unfinished Ti–6Al–4V samples, it appears that an adjustment of cross-sectional area to account for surface roughness can entirely account for the difference in strengths. This presents an interesting comparison between the relatively brittle Ti–6Al–4V and the highly ductile 17–4 PH. The surface

Fig. 8 Comparison of structure of the 17–4 PH and Ti–6Al–4V unfinished samples in the *center* (**a** and **c**, respectively) and at the *edge* (**b** and **d**, respectively)
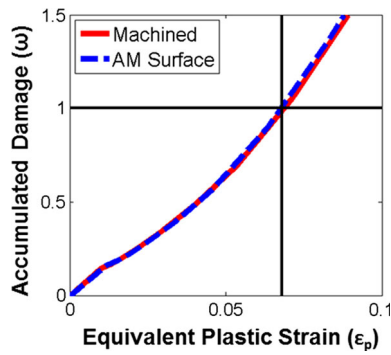
Fig. 9 Comparison of accumulated damage between the unfinished and machined Ti–6Al–4V samples

$$\varepsilon_{\text{crit}} = \ln\left(\frac{1}{1 - \text{ROA}}\right) \tag{1}$$

Once any element in the model reaches the critical strain value, that element is considered to fail. This model was quickly abandoned as it depended on post-test reduction of area measurements which have a high amount of measurement error, and rely largely on equivalent plastic strain which is an aggregate value that is independent of direction. Next a simple stress triaxiality model was implemented [28]. Here, stress triaxiality is calculated from Eq. 2.

$$\sigma_{\text{T}} = \frac{\sigma_1 + \sigma_2 + \sigma_3}{3\sigma_e}, \tag{2}$$

where $\sigma_1, \sigma_2, \sigma_3$ are the principle stresses and σ_e is the Von Mises equivalent stress. This is then used to determine a failure strain which is related exponentially to the stress triaxiality (Eq. 3).

$$\varepsilon_{\text{f}} \propto \exp(-\alpha\sigma_{\text{T}}). \tag{3}$$

A cumulative damage value (ω) is then calculated as the ratio of equivalent plastic strain and failure strain as shown in Eq. 4.

$$\omega = \sum \frac{\Delta\varepsilon_{\text{p}}}{\varepsilon_{\text{f}}} \tag{4}$$

The results of the stress triaxiality model showed no effect of the surface finish, as it was captured by the CMM results, on the elongation to failure. As shown in Fig. 9, when Eq. 4 is fit to the failure data for the machined sample, there is very little deviation between it and the failure prediction of the unfinished sample. It is important to note that the only data used to fit the model parameters were from the machined samples and thus is an incomplete fit. This should not impact the difference between the machined and finished results as the model should be independent of geometry.
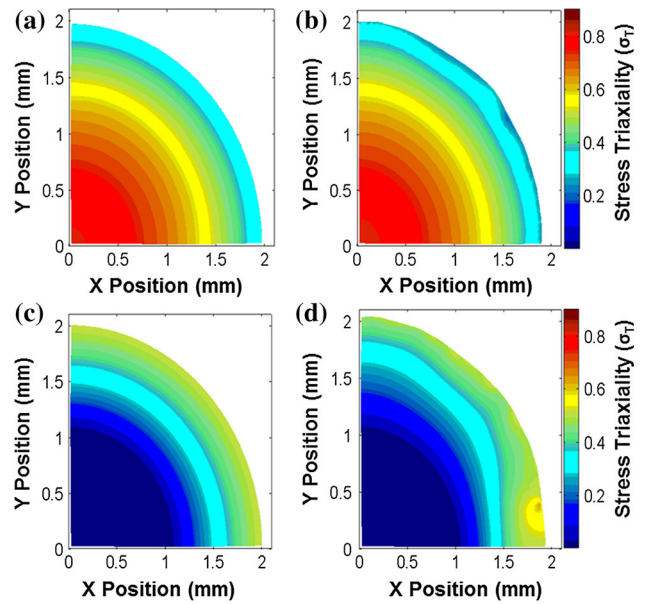

Fig. 10 Comparison of local stress triaxiality between unfinished (right) and machined (left) Ti–6Al–4V simulations at the initiation of failure. a and b are in the regions where failure is predicted to initiate, while c and d are in the regions of the highest surface stress

Upon examination of the location of failure initiation predicted by Eq. 4, it can be seen that both the machined and unfinished sample FEA models reach critical stress triaxiality in the center of the cross-sectional area as would normally be the case for standard ductile failure (Fig. 10). The portion of the unfinished sample that had the highest concentration of surface stress triaxiality at the time of failure was not at the center of the gage length and had a lower magnitude than the center of the predicted failure region.

In order to further explore the potential causes of the difference in elongation to failure of the various samples, fractography was performed. No evidence of failure modes other than ductile rupture initiated failure in the center of the sample with a shear lip was found in the 17–4 PH samples. In the Ti–6Al–4V samples, several clear examples were seen with changes in fracture morphology at the surface of the sample (Fig. 11). At the edge of the sample, evidence of equiaxed ductile rupture can be seen next to shear lip facture.

Since the model and experimental results do not match, closer examination of the surface finish representation used in the model was performed. As shown in Fig. 12, the CMM results did not completely capture the roughness of the surface, and therefore it is likely that the inaccuracy of the model is largely due to the inaccuracy of the modeled geometry.

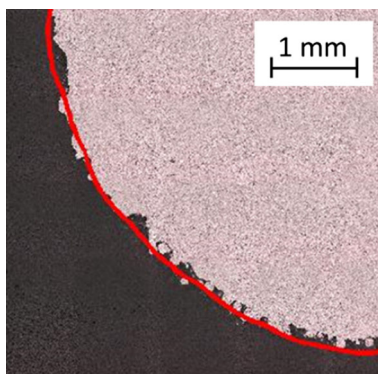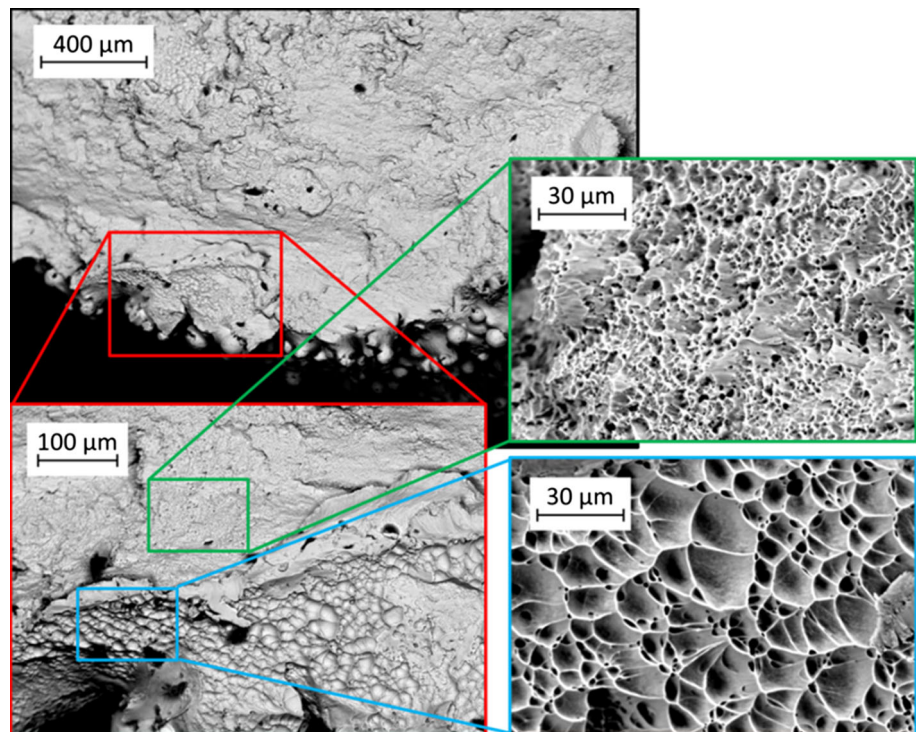**Fig. 11** Fractography of unfinished Ti–6Al–4V SN8 along the edge of the sample

Fig. 12 Comparison of the true cross section of a representative unfinished Ti–6Al–4V sample and the CMM measurement results in *red*

Conclusions

This study focuses on evaluating the difference in behavior between unfinished and machined additively manufactured tensile bars made from both SLM 17–4 PH and EBM Ti–6Al–4V. Experimental results show that an unfinished tensile bar will exhibit lower yield strength with both materials, but ultimate tensile strength is only lower on Ti–6Al–4V samples which exhibit a rougher surface finish. Through CMM measurements, surface roughness measurements, and FEA, the differences in strength is shown to correlate well to error in cross-sectional area measurement on the rough surfaces, though the surfaces of the more ductile 17–4 PH samples show a reduction in stress concentration at the surface as overall strain increases. There is also a significant difference in elongation to failure between the machined and unfinished samples of both materials. Fractography revealed no fracture change in the 17–4 PH samples, but clear indications of ductile rupture are apparent at the surface of the Ti–6Al–4V sample. Attempts to model the rough surface of the samples with a stress triaxiality model were unsuccessful due to incomplete characterization of the samples surface. Overall, improvements need to be made to the surface characterization process, additional data such as various notched tensile samples need to be captured to fully implement the stress triaxiality model, and true stress, true strain data needs to be captured from experiments to reduce model error in the plastic region.

retains and the publisher, by accepting the article for publication, acknowledges that the United States Government retains a non-exclusive, paid up, irrevocable, world-wide license to publish or reproduce the published form of this manuscript, or allow others to do so, for the United States Government purposes.

Compliance with ethical standards

Conflict of Interest The authors declare that they have no conflict of interest.

References

1. El-Hajje A, Kolos EC, Wang JK, Maleksaeedi S, He Z, Wiria FE, Ruys AJ (2014) Physical and mechanical characterization of 3D-printed porous titanium for biomedical applications. J Mater Sci 25(11):2471–2480. doi:10.1007/s10856-014-5277-2
2. Hrabe N, Quinn T (2013) Effects of processing on microstructure and mechanical properties of a titanium alloy (Ti–6Al–4V) fabricated using electron beam melting (EBM), part 1: distance from build plate and part size. Mater Sci Eng, A 573:264–270
3. Zhang LC, Klemm D, Eckert J, Hao YL, Sercombe TB (2011) Manufacture by selective laser melting and mechanical behavior of a biomedical Ti–24Nb–4Zr–8Sn alloy. Scr Mater 65(1):21–24
4. Kempen K, Yasa E, Thijs L, Kruth JP, Van Humbeeck J (2011) Microstructure and mechanical properties of selective laser melted 18Ni-300 steel. Phys Procedia 12:255–263
5. Xu W, Brandt M, Sun S, Elambasseril J, Liu Q, Latham K, Qian M (2015) Additive manufacturing of strong and ductile Ti–6Al–4V by selective laser melting via in situ martensite decomposition. Acta Mater 85:74–84
6. Mathisen MB, Eriksen L, Yingda YU, Jensrud O, Hjelen J (2014) Characterization of microstructure and strain response in Ti–6Al–4V plasma welding deposited material by combined EBSD and in situ tensile test. Trans Nonferr Met Soc China 24(12):3929–3943
7. Wang F (2012) Mechanical property study on rapid additive layer manufacture Hastelloy® X alloy by selective laser melting technology. Int J Adv Manuf Technol 58(5–8):545–551
8. Zhu Y, Li J, Tian X, Wang H, Liu D (2014) Microstructure and mechanical properties of hybrid fabricated Ti–6.5 Al–3.5 Mo–1.5 Zr–0.3 Si titanium alloy by laser additive manufacturing. Mater Sci Eng, A 607:427–434
9. Suo H, Chen Z, Liu J, Gong S, Xiao J (2014) Microstructure and mechanical properties of Ti-6Al-4V by electron beam rapid manufacturing. Rare Metal Mater Eng 43(4):780–785
10. Ram GJ, Esplin CK, Stucker BE (2008) Microstructure and wear properties of LENS® deposited medical grade CoCrMo. J Mater Sci 19(5):2105–2111. doi:10.1007/s10856-007-3078-6
11. Chen J, Xue L, Wang SH (2011) Experimental studies on process-induced morphological characteristics of macro-and microstructures in laser consolidated alloys. J Mater Sci 46(17):5859–5875. doi:10.1007/s10853-011-5543-3
12. Hrabe N, Quinn T (2013) Effects of processing on microstructure and mechanical properties of a titanium alloy (Ti–6Al–4V)
13. Bass BS (2008) Validating the Arcam EBM process as an alternative fabrication method for titanium-6Al-4V alloys. http://www.lib.ncsu.edu/resolver/1840.16/2757. Accessed 17 Dec 2015
14. Ackelid U, Svensson M (2009) Novel sintering approaches: additive manufacturing of dense metal parts by electron beam melting, European Congress and exhibition on powder metallurgy. In: European PM conference proceedings, pp 1–6
15. Antonysamy AA (2012) Microstructure, texture and mechanical property evolution during additive manufacturing of Ti6Al4V alloy for aerospace applications. PhD Dissertation, University of Manchester
16. Spierings AB, Herres N, Levy G (2011) Influence of the particle size distribution on surface quality and mechanical properties in AM steel parts. Rapid Prototyping J 17(3):195–202
17. Kruth JP, Mercelis P, Van Vaerenbergh J, Froyen L, Rombouts M (2005) Binding mechanisms in selective laser sintering and selective laser melting. Rapid prototyping journal 11(1):26–36
18. Vilaro T, Colin C, Bartout JD, Nazé L, Sennour M (2012) Microstructural and mechanical approaches of the selective laser melting process applied to a nickel-base superalloy. Mater Sci Eng, A 534:446–451
19. Rafi HK, Karthik NV, Gong H, Starr TL, Stucker BE (2013) Microstructures and mechanical properties of ti6al4v parts fabricated by selective laser melting and electron beam melting. J Mater Eng Perform 22(12):3872–3883
20. Niendorf T, Brenne F (2013) Steel showing twinning-induced plasticity processed by selective laser melting—An additively manufactured high performance material. Mater Charact 85:57–63
21. Suh CH, Jung YC, Kim YS (2010) Effects of thickness and surface roughness on mechanical properties of aluminum sheets. J Mech Sci Technol 24(10):2091–2098
22. Chen L, Ahadi A, Zhou J, Ståhl JE (2013) Modeling effect of surface roughness on nanoindentation tests. Procedia CIRP 8:334–339
23. Xie HB, Manabe K, Jiang ZY (2013) A novel approach to investigate surface roughness evolution in asymmetric rolling based on three dimensional real surface. Finite Elem Anal Des 74:1–8
24. ASTM Standard E8 (2015) standard test methods for tension testing of metallic materials, ASTM International, West Conshohocken. doi: 10.1520/E0008-15A, www.astm.org
25. ASTM Standard E4 (2014) Standard practices for force verification of testing machines, ASTM International, West Conshohocken. doi: 10.1520/E0004-14, www.astm.org
26. ASTM Standard E83 (2010) Standard practice for verification and classification of extensometer systems, ASTM International, West Conshohocken. doi:10.1520/E0083-10A, www.astm.org
27. Metallic materials properties development and standardization (MMPDS-01). U.S. Department of Transportation
28. Oh CS, Kim NH, Kim YJ, Baek JH, Kim YP, Kim WS (2011) A finite element ductile failure simulation method using stress-modified fracture strain model. Eng Fract Mech 78(1):124–137